Title Page:

Title: Multi-Decadal Convection-Permitting Climate Projections for China's Greater Bay Area and Surroundings

Author names and affiliations: Y. Qing[1] and S. Wang[1,2,*]

[1]Department of Land Surveying and Geo-Informatics, The Hong Kong Polytechnic University, Hong Kong, China

[2]The Hong Kong Polytechnic University Shenzhen Research Institute, Shenzhen, China

[*]Corresponding author. Phone: (852) 3400-3896; Email: shuo.s.wang@polyu.edu.hk

Abstract

The Guangdong-Hong Kong-Macao Greater Bay Area (GBA) is the world's largest bay area in terms of land area and population, which has been increasingly suffering from weather and climate extremes under global warming. It is thus desired to produce reliable high-resolution climate information at a regional scale in order to enhance resilience to climate change over the GBA. For the first time, this study develops the multi-decadal nested-grid climate projections at a convection-permitting scale for the GBA, and assesses the abilities of the Weather Research and Forecasting (WRF) model with 36-, 12- and 4-km resolutions in representing precipitation, temperature and their extremes. Our findings indicate the added value of the convection-permitting WRF model for simulating the spring and summertime precipitation as well as extreme heavy rainfall events with daily amounts larger than 30 mm over the GBA. Increasing the spatial resolution of the WRF model does not necessarily lead to a significant improvement on temperature simulations. In addition, our findings reveal that the GBA is expected to experience an increasing number of heavy and extreme heavy rainfall events by the end of the 21st century. Moreover, the GBA is projected to experience a large temperature change across different seasons, and an enhanced warming will appear in autumn. The GBA is also expected to have more summer days with longer durations, thereby leading to an increasing risk of heatwaves and heat stress.

Keywords Greater Bay Area; Regional climate; Convection permitting; Temperature; Precipitation; Extremes

1 Introduction

The changing climate leads to increasingly frequent and severe weather extremes in recent years, which have been widely observed around the world (Fischer and Knutti 2015; Miao et al. 2016). These extreme events have been posing significant threats to agricultural production, human health, ecosystems and the environment (Intergovernmental Panel on Climate Change 2013). For example, extreme events such as floods, droughts, heat waves, and other natural disasters killed over 1.2 million and affected 2.5 billion people worldwide from 1991 to 2005 (Centre for Research on the Epidemiology of Disasters 2005). During the same period, conservative estimates indicate that global natural disasters have caused more than $1.3 trillion dollars in economic losses associated with damages to properties and crops (Huppert and Sparks 2006; Mayhorn and McLaughlin 2014). Climate simulations and projections play a crucial role in advancing our understanding of temporal and spatial changes in climate variables as well as the resulting consequences so as to develop climate change mitigation and adaptation strategies for reducing potential losses from the climate-induced natural disasters.

Global climate models (GCMs) are recognized as an effective tool to simulate climate change scenarios (Hagemann et al. 2011; Svensson et al. 2015; Bennett et al. 2016; Pfahl et al. 2017; Sun et al 2017; Wang and Zhu 2020). However, GCMs cannot be used to simulate regional-scale climate features and variations, especially for complex terrain such as urban and mountainous regions. Dynamical downscaling is thus needed to produce the high-resolution climate information for conducting regional climate change impacts studies. Regional climate models (RCMs) is a typical dynamical downscaling approach that can transform the coarse-resolution outputs of GCMs to the higher-resolution climate information. Tremendous efforts have been made to conduct high-resolution climate simulations using RCMs over the past decades (Caldwell et al. 2009; Heikkilä et al. 2011; Lavender and Walsh 2011; White et al. 2013; Yu et al. 2015; Zhu et al. 2019). Nevertheless, RCMs with a typical spatial resolution of 25−50 km cannot resolve deep convection and associated precipitation. It is found that the horizontal resolutions of 25–50 km are insufficient to represent fundamental and persistent atmospheric processes associated with the convective boundary layer or the irregular coastlines and topography (Kanamitsu and Kanamaru 2007). Convection parameterization schemes (Kang and Hong 2008; Clark et al. 2016; Ishida et al. 2020) are thus used to approximate the convection processes in RCM simulations for improving the accuracy of dynamical downscaling. However, the convection parametrization is considered as the major source of model uncertainties and errors, which may result in the misrepresentation of convective precipitation processes (Prein et al 2015).

To provide more realistic high-resolution climate information at a regional scale, especially for complex topographic regions, the convection-permitting modeling (CPM) has been receiving increasing attention due to its ability to explicitly resolve local-scale forcing and processes associated with complex topography and land cover in response to variability in the large-scale atmospheric circulation (Liu et al. 2011; Rasmussen et al. 2014; Silverman et al. 2013; Kendon et al. 2017; Leutwyler et al. 2017; Liu et al. 2017; Prein et al. 2017; Chan et al. 2018; Wagner et al. 2018; Chen et al 2020; Kouadio et al. 2020). The CPM with horizontal grid spacing of less than 4 km is able to explicitly resolve convection without the use of convection parameterization schemes, which largely improves the representation of orography and variations of surface fields at an ultra-high spatial resolution. This can be particularly advantageous for urban and mountainous regions with heterogeneous land surfaces. In addition, dynamical downscaling through the nested regional climate modeling system shows relatively high skills in representing land surface characteristics as well as fine-scale climate features and extreme events (Frei et al. 2006; Salathe et al. 2008; Brisson et al. 2016). For example, Zittis et al. (2017) and Qiu et al. (2020) provided evidence that the nested domain was better able to simulate sharp temperature gradients and extreme rainfall events. To assess the kilometer-scale CPM with multiple nested grids for performing regional climate simulations over complex terrain, its added value was thus examined.

According to the Fifth Assessment Report of the Intergovernmental Panel on Climate Change (IPCC AR5), human society will become much more vulnerable to weather and climate extremes by the end of the 21st century as a consequence of continuous global warming, with global temperature increasing by 1.1–6.4 °C relative to 1980–1999. Moreover, the frequency and intensity of extreme precipitation events have been obviously increasing in many countries (Bao et al. 2015; Kim et al. 2020; Kirchmeier-Young and Zhang 2020). The dramatic increases in temperature and precipitation extremes have a substantial impact on human society, ecosystems, and the environment. Therefore, projecting and understanding future climate change play an important role in driving sustainable development initiatives in a warming climate.

The GBA is a city cluster consisting of nine cities in Guangdong Province and two Special Administrative Regions (Hong Kong and Macau), which is the world's largest bay area in terms of land area and population. Along with the Belt and Road Initiative, the development of the GBA is a major initiative driven by the Chinese government. The GBA has a typical subtropical monsoon climate with the frequent occurrence of meteorological disasters caused by extreme weather, and the resulting economic losses account for more than 80% of total losses from natural disasters (Gao et al. 2020). Furthermore, the GBA has been increasingly suffering from weather and climate extremes due to global warming and rapid urbanization, which has been posing severe impacts on human society and the environment in populous urban areas (Hallegatte et al. 2013; Swiss 2013). Little effort has been made to produce reliable high-resolution climate change information for the GBA. It is thus desired to project the spatial and temporal evolution of the changing climate and to assess potential climate change impacts for build a climate-resilient city cluster over the GBA.

For the first time, the multi-decadal convection-permitting climate projection with horizontal grid spacing of 4 km will be conducted in this study for the GBA with complex terrain. The nested-grid WRF model simulations with different horizontal resolutions will be carried out for two different time periods, including a baseline period from 1980 to 2005 and a future period from 2074 to 2099. The WRF model simulations will be validated and compared across different spatial resolutions. The added values of the multi-decadal convection-permitting climate simulation will also be examined systematically by comparing against observations. In addition, future changes of precipitation, temperature and their extremes will be projected for the GBA under the Representative Concentration Pathways 8.5 (RCP8.5) scenario. RCP8.5 corresponds to a high greenhouse gas emissions pathway, which can be called 'baseline' scenario that does not include any specific climate mitigation target (Riahi et al. 2011).

This paper is organized as follows. Sect. 2 describes the study area, the experimental design, the evaluation metric, as well as the data source and deposit. Sect. 3 presents the evaluation and comparison of the present-day WRF model simulations across different spatial resolutions as well as the projected changes of precipitation, temperature and their extremes. Sect. 4 summarizes the key findings and main conclusions drawn from this study.

2 Experimental Design and Data

2.1 Description of the study area

The GBA is located between 21.3ºN–24.2ºN and 111.2ºE–115.3ºE, which covers nine cities (Guangzhou, Shenzhen, Zhuhai, Foshan, Huizhou, Dongguan, Zhongshan, Jiangmen, Zhaoqing) and two Special Administrative Regions of Hong Kong and Macau. It has a total area of 56,000 km^2, with a population of 70 million. The GBA is the world-class urban agglomeration, which is one of the regions with the strongest economic influence in China. Climate change has a substantial impact on the development of regional economy. Thus, an in-depth analysis of climate characteristics plays an important role in understanding the changing climate and potential consequences over the GBA, which provides a solid foundation for developing sound climate change adaptation and mitigation policies.

The GBA has a humid subtropical climate with mild winters (mean temperature of 14.6 °C) and hot summers (mean temperature of 27.9 °C) as well as plentiful rainfall (mean precipitation of 5.2 mm/day), which has complex topography and varying natural conditions (these were calculated based on the weather station data during the period of 1980−2005, provided by the National Meteorological Information Center of China). In recent years, the city cluster of the GBA has been suffering from the increasing extreme events such as heat waves, floods and storm surges induced by the warming climate, which poses a substantial challenge to the sustainable development of the GBA. It is thus desired to provide reliable climate information and to advance the understanding of the changing climate through high-resolution multi-decadal climate model simulations for building a climate-resilient city cluster over the GBA.

2.2 Convection-permitting modeling

The WRF (Skamarock et al. 2005) model was used to perform the multi-decadal convection-permitting climate projections over the GBA and surroundings (hereinafter referred to as the GBA). The WRF features multiple options for boundary layers, convection, microphysics, and radiation as well as land surface model choices, with fully compressible, nonhydrostatic equations solved in the dynamical core, it is thus suitable for simulating a wide range of scales from thousands of kilometers to a few meters. Recent studies have shown that the WRF model can be used to downscale the reanalysis data to a high-resolution horizontal spacing of 4 km (Liu et al. 2017; Prein et al. 2017; Wang and Wang 2019; Zhang et al. 2019; Kouadio et al. 2020). Due to a large number of available options related to the model core and physical parameterization schemes, the WRF model can be configured properly to carry out long-term climate simulations at a regional scale.

In this study, the WRF model was configured with a two-way scheme of three nested grids (Figure 1). The parent domain D01 covers a large part of China with 68 × 56 grid points at a 36-km resolution, which can reduce spurious boundary effects in the inner region (Soares et al. 2014). The nested domain D02 consists of 138×96 grid points at a resolution of 12 km. The innermost domain D03 that covers the GBA with 216×171 grids has a 4-km grid spacing which is fine enough to explicitly resolve the convection processes and to better simulate the details of complex terrain such as the coastlines, mountainous and urban areas (Kouadio et al. 2020). In two-way nesting, the coarse- and fine-resolution simulations are run simultaneously. The coarse-resolution simulation provides boundary values for the fine domain, and the fine-resolution simulation feeds its calculation back to the coarse domain. Such a two-way nesting strategy is able to bring the mesoscale information back from the D03 to upper domains, which is also expected to improve the D01 and D02 performance. The number of vertical levels in the WRF model was 21, with the 50 hPa model top. The initial and lateral boundary conditions were provided by the ERA-Interim reanalysis product at the 0.75º × 0.75º resolution and were updated every 6 hours.

The WRF model was configured properly with the Kain-Fritsch cumulus parameterization (Kain and Fritsch 1992; Kain 2004), the Yonsei University planetary boundary scheme (Hong and Pan 1996), the Monin-Obukhov similarity surface layer scheme (Jimenez et al. 2012), the Rapid Radiative Transfer Model long-wave radiation schame (Mlawer et al. 1997; Iacono et al. 2008), and the Dudhia short-wave radiation schame (Dudhia 1989). Three domains share the same physics parameterizations except that in the innermost domain D03, convective parameterization is not activated to allow explicit convection. Cloud microphysical processes can affect the conditions for the occurrence and development of cumulus convection by adjusting temperature and humidity, and subsequently influence the prediction of precipitation (Lohmann and Roeckner 1996; Morrison and Gettelman 2008). Therefore, choosing different cloud microphysics schemes has a substantial impact on the performance of precipitation simulation. As a result, three different cloud microphysics schemes were examined through sensitivity analysis, including the Lin scheme (Lin et al. 1983), the WRF Single-Moment (WSM) 3-class simple ice scheme, and the WRF Single-Moment (WSM) 5-class scheme (Hong et al. 2006).

To identify the optimal cloud microphysics scheme, a sensitivity investigation was conducted based on a 3-month simulation for the summer season (from June 1 to August 31, 1981). Temporal variations of temperature and precipitation were examined for each sensitivity experiment by comparing against observations under various microphysics parameterizations. As shown in Figure 2, the temporal variations of temperature generated using different microphysics parameterizations are similar to each other, and all the resulting curves match well with observations. Since there is a slight difference between these microphysics parameterizations, it is difficult to identify an optimal scheme based on the performance of temperature simulation. In comparison, precipitation is more sensitive to microphysics parameterizations, thereby leading to a substantial difference in the temporal variations of daily precipitation. Even though all different microphysics parameterizations capture the overall trend of daily precipitation, there are different levels of ability in capturing heavy precipitation days. It can be seen that the WSM5 outperforms Lin and WSM3 in terms of the accuracy in simulating heavy precipitation. The WSM5 scheme was thus selected as the optimal cloud microphysics parameterization of the WRF model.

The multi-decadal convection-permitting climate projection for the future period of 2074−2099 was also forced with the ERA-Interim reanalysis product, and the initial and boundary conditions were consecutively perturbed using the Pseudo-Global Warming (PGW) technique (Liu et al. 2017). The perturbed physical fields include temperature, geopotential, specific humidity, horizontal wind, sea surface temperature, sea level pressure, and soil temperature. As shown in Eq. (1), the climate perturbation was estimated through a multi-model ensemble mean climate change signal. The ERA-Interim reanalysis product was then perturbed every 6 hours by the derived climate change signal to provide the WRF model with initial and boundary conditions for the future climate projection. The future climate projection was developed based on the outputs of the Coupled Model Intercomparison Project Phase 5 (CMIP5) GCMs under the emission scenario of RCP8.5.

$$\mathrm{WRF_{input}} = \text{ERA-Interim} + (\mathrm{CMIP5}_{2071-2100} - \mathrm{CMIP5}_{1976-2005}). \tag{1}$$

To minimize the influence of model uncertainties in quantifying the climate response to future greenhouse gas forcing, we used a multi-model ensemble mean climate difference between past and future periods. A total of 10 CMIP5 GCMs were selected based on their performance in simulating the climate over China. Details of these 10 GCMs are provided in Table S1 of the supplementary material.

2.3 Evaluation metric

The WRF model climate simulations were evaluated based on weather station data (Table S2 of the supplementary material). The model outputs with three nested grids (36-, 12- and 4-km) match the grid data to the corresponding or nearest station. To assess the performance of climate simulations across different resolutions, the added value (AV) was computed using Eq. (2) proposed by Di Luca et al. (2013):

$$AV = \frac{(M_1 - O)^2 - (M_2 - O)^2}{Max((M_1 - O)^2, (M_2 - O)^2)} \tag{2}$$

where M_1 is the WRF-simulated values with the relatively coarse resolution, M_2 denotes the WRF-simulated values with the relatively high resolution, and O is the observational data obtained from weather station data. The AV is positive when the M_2*'s* squared error is smaller than the M_1*'s* one and negative otherwise. The positive values suggest an improvement of model performance by M_2, while the negative values indicate that M_2 degrades model performance achieved by M_1.

2.4 Data source and deposit

The APHRODITE dataset (Yatagai et al. 2012) is equipped with two different resolutions (0.25° and 0.5°) of daily precipitation and temperature during 1951–2018, and the dataset is provided for several regions of Asian. This dataset is created by collecting and analyzing gauge observations across Asia through the activities of the APHRODITE's water resources project. To validate the WRF model simulations, the 0.25º × 0.25º daily gridded precipitation and temperature datasets were collected from APHRODITE and ERA-Interim reanalysis product for the period 1980–2005. Apart from these datasets, the ground-based observations of daily precipitation and temperature were collected from weather stations over the study area to compute the added values of the WRF-4km simulation in comparison with WRF-12km and WRF-36km simulations, which are considered more reliable than other reanalysis products. The meteorological data was provided by the National Meteorological Information Center of China (http://data.cma.cn/site/index.html).

A web-based data portal, known as China's Greater Bay Area Climate Data Portal (GBAcdp), was also developed in this study to make the simulated and projected climate information available to the public (http://www.gbacdp.cn/). The GBAcdp provides visual representations of the convection-permitting WRF model outputs in the forms of long-term trends, averages, and extremes using interactive web maps, which enables both technical and nontechnical users to have an easy access to the high-resolution climate data. The home page of the GBAcdp was designed with a user-friendly layout. And a number of auxiliary functions were provided to facilitate map viewing or downloading the data for the selected area.

As shown in Figure 3a, the GBAcdp consists of three main modules: user access, main panel, and map overview. The user access module is designed to facilitate quick and easy access to the data portal. The access to GBAcdp is free of charge and without a login requirement, but users are required to create an account to download data. The main panel provides an easy way for users to view different pages and data. And the map overview allows users to efficiently view high-resolution maps of climatic variables (e.g., temperature and precipitation) over the GBA. Specifically, users can freely explore the interactive maps with more than 30,000 grids over the GBA. In addition, the average annual climatic variables are derived for the historical period of 1980−2005 and the future period of 2074−2099, which are shown in the form of time series for each of 11 cities over the GBA. As shown in Figure 3b, the GBAcdp can provide the time series of average annual precipitation and temperature for each GBA city, which allows users to download the time series data. Temporal and spatial changes in climate variables play an important role in addressing climate change mitigation and adaptation. More gridded datasets of climatic variables and extreme indices will be released in the near future to facilitate the strengthening of research and policy on adaptation to climate change over the GBA.

3 Results and Discussion

3.1 Evaluation of precipitation and temperature simulations with three nested grids

To evaluate the performance of the WRF model with three nested grids, the WRF simulations with horizontal grid spacing of 36 km (WRF-36km), 12 km (WRF-12km), and 4 km (WRF-4km) were compared against each other over the GBA (domain D03). Figure 4 shows the comparison of absolute and relative model biases for the average daily precipitation simulations with 36-, 12- and 4-km resolutions. It can be seen that all simulations exhibit a consistent spatial pattern of model biases, which shows a wet bias of 3 mm/day in the north of the GBA and a dry bias of 2 mm/day in the south. Specifically, the WRF-36km and WRF-12km simulations exhibit a domain-averaged wet bias of 1.7 and 1.5 mm/day, respectively. In contrast, the WRF-4km simulation shows a relatively small domain-averaged wet bias of 0.4 mm/day. These indicate that the convection-permitting WRF-4km simulation is able to better capture daily precipitation over the GBA due to the explicit representation of convection processes associated with orographic features in comparison with the WRF-36km and WRF-12km simulations.

Figure 5 assesses the skill of the WRF model in simulating seasonal precipitation across different resolutions over the GBA. In comparison, the WRF-4km simulation has better representation of both spatial and temporal evolution of precipitation in spring and summer, with a smaller model bias (Figure 5a). The distribution of seasonal daily precipitation also shows better performance of the WRF-4km in simulating spring and summertime precipitation (Figure 5b). However, the WRF model with different spatial resolutions shows similar biases in simulating winter and autumn precipitation over the GBA. These are further confirmed by the Taylor diagram (Figure 6) that shows the correlation coefficient (COR), standard deviation (SD), and root-mean-square error (RMSE) between simulated and observed precipitation patterns in a graphical way. The WRF model with different resolutions exhibits similar performance in simulating the spatial distribution of autumn precipitation. Except for the autumn precipitation simulation, the convection-permitting WRF-4km simulation shows better skills of reproducing the spatial pattern of seasonal precipitation, especially for the spring and summertime precipitation simulations with the higher CORs and the lower RMSEs compared to those derived from the WRF-36km and WRF-12km simulations. This verifies that the convection-permitting climate simulation is crucial to improving the accuracy of capturing the precipitation patterns in warm seasons (MAM and JJA).

Figure 7 shows the comparison of simulated and observed monthly and annual precipitation time series. Our findings indicate that the WRF simulations with three different resolutions are able to capture the interannual variations in precipitation over the GBA, with the maximum monthly precipitation observed in June and a predominant increase in annual precipitation from 1991 to 1992. The WRF simulations have wet biases from March to September, with a maximum bias of 3.9 mm/day in June derived from the WRF-36km simulation. This is mainly due to a considerable overestimation in the simulated summertime precipitation in the north of the GBA. In comparison, the temporal variations of monthly and annual precipitation simulated with the 4-km resolution are in better agreement with observations, thereby leading to smaller biases than those generated from the WRF-36km and WRF-12km simulations.

In addition to the evaluation of precipitation simulations across different temporal scales, the skill of the WRF model in simulating surface air temperature was also examined across three different resolutions. Figure 8 depicts the spatial patterns of absolute and relative model biases for the daily mean temperature simulations with 36-, 12- and 4-km resolutions. In general, the spatial distributions of simulated daily mean temperatures are similar across different resolutions. Due to the orographic features, daily temperatures are characterized by a north–south gradient over the GBA. As expected, the temperature is relatively low for the mountainous areas at high altitudes. The temperature increases gradually from north to south, which is consistent with the changing trend of the observed temperature. In comparison, the WRF model with the 4-km spatial resolution is able to produce more details (e.g., small-scale hotspots of low temperatures in the north, as shown in Figure S1) in the spatial pattern of temperature changes, whereas the WRF-36km simulation shows much less details in the varying temperature pattern. As depicted in Figure 8, the differences of daily mean temperatures simulated across different resolutions are rather small. Specifically, the WRF-4km simulation has the domain-averaged absolute and relative model biases of –0.4 °C and –1.9%, respectively. In comparison, the WRF-36km and WRF-12km simulations generate slightly larger domain-averaged model biases. Overall, increasing the spatial resolution of the WRF model does not necessarily lead to a significant improvement on daily temperature simulations over the GBA due to the rather small differences of daily mean temperatures simulated across different resolutions. Likewise, the convection-permitting climate simulation does not show a pronounced improvement on seasonal temperature simulations (Figure 9). The similar biases and distributions of simulated seasonal temperatures are derived from the WRF model simulations with different spatial resolutions.

Figure 10 depicts a comparison between simulated and observed time series of monthly and annual mean temperatures for the period from 1980 to 2005. It can be seen that there is an underestimation in the simulated monthly mean temperature across all resolutions, with the relatively large bias that appears from June to September. Such a dry bias is partly due to an underestimation of summertime temperatures simulated at different resolutions. Overall, the differences among three different simulations are rather small, and the annual temperature curves match well with each other. As for the trend of annual mean temperature, the WRF-36km and WRF-12km simulations show an underestimation during the period from 1980 to 2005, with relatively large biases that appear in 1998 (0.8 °C) and 2003 (0.9 °C). In contrast, the WRF-4km simulation is much closer to the observation, with an average bias of 0.1 °C. This indicates that the convection-permitting WRF-4km shows higher skills of capturing the monthly and annual mean temperature trends when compared with WRF-36km and WRF-12km.

3.2 Added values of precipitation and temperature simulations

To further examine the skills of the convection-permitting WRF model, we assess the added values (AVs) of the WRF-4km simulation of annual and summer precipitation and temperature relative to the WRF-36km and WRF-12km simulations. As shown in Figure 11, the AVs of the WRF-4km simulation against the WRF-36km and WRF-12km simulations are computed using the weather station data as the reference dataset. Most AVs of the WRF-4km against the WRF-36km are positive (Figures 11b and d), indicating that the WRF-4km has better skills of simulating precipitation. Compared with the WRF-36km simulation, there is a relatively small improvement of the WRF-4km against the WRF-12km (Figures 11a and c). It should be noted that the WRF-4km simulation shows a pronounced improvement in the northwest of the GBA in summer, especially for the WRF-4km simulation against the WRF-36km simulation in which a considerable wet bias exists due to a large overestimation in the High Plains during the summer season (Figure 4). Generally, the summertime precipitation is rather difficult to simulate since precipitation is concentrated in the summer months when the monsoon prevails, which could result in a considerable bias of annual precipitation simulation. Thus, improving the simulation of warm-season precipitation plays a crucial role in improving the reliability of precipitation simulation. It is also important to note that the WRF-4km shows better skills of simulating precipitation over the northwest parts of the GBA, indicating that the convection-permitting WRF model is able to improve the representation of precipitation pattern over complex terrain.

Compared with precipitation simulations, there is no apparent differences in temperature simulations across different resolutions. Figures 11e-h show the AVs of annual and summertime temperature simulations. On average, there is no obvious improvement by the WRF-4km simulation compared to the WRF-36km and WRF-12km simulations. These indicate that the use of the convection permitting WRF model can lead to a noticeable improvement on precipitation simulations but not necessarily for simulating temperatures over the GBA.

3.3 Evaluation of extreme precipitation and temperature simulations

In addition to a thorough evaluation of daily, seasonal and annual precipitation and temperature simulations across different resolutions, the WRF model simulations of precipitation and temperature extremes were also assessed using various extreme indices. The precipitation extreme indices include the simple daily intensity index (SDII) and the consecutive wet days (CWD). The temperature extreme indices include the number of summer days (SU) and the consecutive summer days (CSU). A detailed description of precipitation and temperature extreme indices is provided in Table 1.

3.3.1 Extreme precipitation

The precipitation extreme indices (SDII and CWD) derived from the WRF simulations with different resolutions (WRF-36km, WRF-12km, and WRF-4km) are validated against those derived from observations. As shown in Figures 12a-c, all WRF simulations tend to overestimate the values in most areas of the GBA. In contrast, the WRF-4km simulation improves the representation of the SDII by reducing the positive bias in the north. According to regional statistics of the SDII derived from different simulations and the observation (see Figure S2 of the supplementary material), the WRF-4km simulation shows the best performance, with the domain-averaged SDII of 12.5 mm/day which is closest to the observational data (13.7 mm/day). As for the CWD, it can be seen that all simulations have a similar spatial distribution with relatively small biases in the central part of the GBA and relatively large biases in the southwest. In contrast, the WRF-4km simulation is able to reduce the biases of the domain-averaged CWD, especially for the considerable biases in the southwest. Overall, there is a consistent pattern of model biases of SDII and CWD simulated across different resolutions, but the WRF-4km simulation has a pronounced improvement on the representation of extreme precipitation indices (SDII and CWD) over the GBA.

Figure 13 presents the frequency distribution of simulated and observed daily precipitation with different intensities. Daily precipitation is divided into 10 categories, including 0−5, 5−10, 10−15, 15−20, 20−30, 30−40, 40−50, 50−60, 60−70, and 70−80 mm/day. Compared with the observational data, the WRF-4km simulation shows a relatively large overestimation on the frequency of daily precipitation ranging from 0 to 5 mm/day and underestimation on those from 5 to 30 mm/day, while the WRF-36km and WRF-12km simulations are closer to the observation (see Table S3 of the supplementary material). Nevertheless, the WRF-4km shows much better skills in capturing the frequency of daily precipitation over 30 mm/day compared to the WRF-36km and WRF-12km simulations. This reveals that precipitation extremes are sensitive to the improvement of model resolution and the representation of convection processes. Thus, the convection-permitting model has higher skills of capturing heavy rainfall events, especially for extreme heavy rainfall events with daily amounts larger than 30 mm over the GBA.

3.3.2 Extreme temperature

Figure 14 depicts the absolute biases of the climatologically averaged counts of SU and CSU derived from the WRF model simulations across different resolutions over the GBA. Compared with the WRF-36km and WRF-12km simulations, the WRF-4km simulation generates smaller biases of SU and CSU, especially for the central part of GBA. The domain-averaged SU and CSU derived from the WRF-4km simulation are 96 and 42 days, respectively. These are in better agreement with the observation in comparison with those derived from the WRF-36km and WRF-12km simulations (see Figure S3 of the supplementary material).

Figure 15 depicts the comparison in the frequencies of simulated and observed daily mean temperatures as well as the observation over the GBA. When the daily mean temperature ranges from 20 to 25 °C, the WRF model simulations with three different resolutions are in agreement with the observation, thereby leading to a relatively small bias. In comparison, the WRF-4km shows better skills in capturing daily mean temperatures higher than 28 °C. This suggests that the convection-permitting model is able to better simulate the high and extreme temperature events even though there is a general underestimation for all simulations across different resolutions.

3.4 Projected changes in precipitation and temperature

Future changes in precipitation and temperature over the GBA are projected for the period of 2074–2099 relative to the reference period of 1980–2005. Figure 16 shows the spatial distributions of the percentage changes in the annual and seasonal precipitation by the end of the 21st century. The annual precipitation over most parts of the GBA is projected to increase slightly for all simulations with different resolutions. Specifically, the domain-averaged percentage increase in the annual precipitation is projected to be 2.1% from the WRF-36km simulation, 2.4% from the WRF-12km simulation, and 4.8% from the WRF-4km simulation, respectively.

The signal of changes in seasonal precipitation is more pronounced for different areas of the GBA. The most pronounced decrease of up to 50% is expected to appear in the west of the GBA during the summer season, whereas winter, spring, and autumn precipitation amounts are projected to generally increase for all simulations. In comparison, the magnitude of increase derived from the WRF-4km simulation is stronger than those from the WRF-36km and WRF-12km simulations, with the domain-averaged values of up to 42.7% in spring and 17.6% in winter. These indicate that the wetting trend over the GBA can be enhanced by the convection-permitting simulation. Furthermore, the autumn precipitation from the WRF-4km simulation shows a positive change of 25.8%, while the WRF-36km and WRF-12km simulations show a negative change of 9.8% and 10.8%, respectively. Such large positive changes in winter, spring and autumn precipitation are mainly due to the fact that the convection-permitting simulation has better skills of simulating extreme rainfall events. For example, the WRF-4km simulation projects a maximum positive change of up to 80% in the north of the GBA, whereas the WRF-36km and WRF-12km simulations show a maximum positive change over the same region but with much smaller values (40% and 50%), as shown in Figures 16 m-o. Although the annual and seasonal precipitation show different growth rates across different resolutions, the overall trends are increasing in winter, spring, and autumn over the GBA.

As shown in Table 2, the rainfall events are divided into six categories, including wet days (above 1 mm/day), light rain (1–10 mm/day), medium rain (10–25 mm/day), large rain (25–50 mm/day), heavy rain (50–80 mm/day), and extreme heavy rain (> 80 mm/day). The occurrence of precipitation intensity below 1 mm/day is projected to decrease considerably for all simulations, with a decline of 5–31 days. In contrast, the frequencies of heavy precipitation (in the range between 50 and 80 mm/day) and extreme heavy precipitation (above 80 mm/day) are projected to generally increase. For example, a total of 4.4 days is expected to experience extreme heavy rainfall events based on the WRF-4km simulation, which is larger than the number of extreme heavy rain days (3.6 days) occurred during 1980–2005. Furthermore, more extreme heavy rain days are projected by the WRF-4km simulation (4.4 days) compared to those from the WRF-36km (2.8 days) and WRF-12km (3.2 days) simulations, as shown in Table 2. Overall, except for summertime precipitation, the amount of future rainfall is projected to increase over the GBA, especially in spring. In addition, the heavy and extreme heavy rainfall events will increase even though the number of wet days is projected to decrease by the end of 21st century. These imply a potential increase in flood risk as a result of the increasing extreme heavy rainfall events over the GBA.

As for the temperature projection, most parts of the GBA are expected to experience a considerable temperature rise of 2.5 to 5.5 °C by the end of this century under the RCP8.5 scenario. All simulations consistently project a domain-averaged increase of 3.7 °C in the annual mean temperature (Figure 17). In addition, the GBA is expected to experience a large temperature change across different seasons, and an enhanced warming will occur in autumn, with a domain-averaged increase of over 4 °C. In comparison, warming will be less pronounced in spring, with a relatively small increase of 3 °C. Overall, the greatest temperature rise is expected in the northern part of the GBA in all seasons, while the southern part will experience a relatively small increase. There will be a domain-averaged temperature increase of over 3 °C based on all simulations with different resolutions. Such a large increase in temperature will have dramatic adverse impacts on human society and nature systems. Urgent actions are thus needed to mitigate global warming, and adaptation measures should also be integrated into the GBA development strategies to enhance society's resilience to extreme weather and climate events under global warming.

3.5 Projected changes in precipitation and temperature extremes

Figure 18 depicts the projected changes of extreme precipitation and temperature indices over the GBA. On average, the SDII is projected to increase over most parts of the GBA, while the CWD is expected to generally decrease, except for a predominant increase in the northwest of the GBA. Specifically, the SDII is projected to increase by up to 1.8 mm/day, which makes a positive contribution to the increase in the annual precipitation. However, the number of wet days is projected to decrease, indicating that the expected increase in total precipitation is mainly due to the increase in precipitation intensity rather than the change in precipitation frequency. Although the precipitation intensity is expected to increase in the future, the duration of precipitation will decrease owing to the domain-averaged negative change of CWD. As shown in Figures 18 a-c, the CWD is projected to decrease by nearly 2 days. Overall, an increase in the amount of precipitation but a decrease in the number of rain days imply an increasing intensity of rainfall events over the GBA. The projected changes in heavy precipitation provide meaningful insights into the flood risk assessment, which plays a crucial role in facilitating policymakers and stakeholders to develop adaptation strategies for reducing potential damages caused by extreme rainfall events.

In addition to the future projection of precipitation extremes, both the frequency and duration of extreme temperature are projected to increase over the GBA. Specifically, the domain-averaged SU values are projected to increase by more than 70 days by the end of the 21st century, and the relatively large changes will mostly occur in the north of the GBA. This indicates that the northern part of the GBA is expected to experience the daytime temperatures above 25 °C during the entire summer season. As for the CSU, there is a noticeable difference in model simulations with different resolutions. The WRF-4km simulation shows an increase of up to 69 summer days relative to the reference period (1980–2005), which is more than those from the WRF-36km (58 days) and WRF-12km (66 days) simulations. Based on the convection-permitting simulation, therefore, the GBA is projected to experience more summer days and longer consecutive summer days. Such an increase in both frequency and duration of summer days is expected to lead to an increase of heatwaves as well as a rising risk of heat stress, which will have substantial negative impacts on agricultural production, water supply, and human health.

4 Summary and conclusions

For the first time, the multi-decadal convection-permitting climate projections with horizontal grid spacing of 4 km were developed for the GBA with complex terrain. Three nested-grid climate simulations with 36-, 12- and 4-km resolutions were carried out and compared against each other in order to explicitly evaluate the performance of the WRF model in regional climate simulations for the GBA across different spatial and temporal scales. Future changes in precipitation, temperature and their extremes are also projected for the period of 2074–2099 relative to the reference period of 1980–2005.

Our findings reveal the added values of the convection-permitting climate simulations with the 4-km resolution for reproducing the spatial pattern of precipitation, especially for the spring and summertime precipitation as well as extreme heavy rainfall events with daily amounts larger than 30 mm over the GBA. Even though the the convection-permitting climate simulation is able to produce more details in the spatial pattern of temperature changes, there is no obvious difffenence in biases and distributions of temepratures simulated across different resolutions. This indicates that increasing the spatial resolution of the WRF model does not necessarily lead to a significant improvement on temperature simulations over the GBA. In contrast, the convection-permitting WRF model is able to better simulate the high and extreme temperature events even though there is a general underestimation for all simulations across different resolutions.

Future climate projections indicate that the GBA is expected to experience an increasing number of heavy and extreme heavy rainfall events by the end of the 21st century, implying a potential increase in flood risk over the GBA. The overall trends in the annual and seasonal precipitation are also increasing except for the summertime precipitation, and the wetting trend can be enhanced by the convection-permitting climate simulation. In addition, the GBA is expected to experience a large temperature change across different seasons, and an enhanced warming will appear in autumn, with a domain-averaged increase of over 4 °C. The northern part of the GBA is expected to experience the greatest temperature rise, while the southern part will experience a relatively small increase. Overall, the GBA is projected to experience more summer days with longer durations. Such an increase in both frequency and duration of summer days will lead to an increase in the risks of heatwaves and heat stress.

It should be noted that the convection-permitting climate projections were developed in this study under the business-as-usual scenario of RCP8.5. The warming trends and climate-related risks would be reduced under the other scenarios such as the most aggressive mitigation scenario of RCP2.6. In addition, the ultra-high resolution meteorological observations (e.g., precipitation) or reanalysis products are much needed to better evaluate the convection-permitting climate simulations with horizontal grid spacing of 4 km over the GBA.

Acknowledgments This research was supported by the National Natural Science Foundation of China (Grant No. 51809223) and the Hong Kong Research Grants Council Early Career Scheme (Grant No. PP5Z). The meteorological data was provided by the National Meteorological Information Center (http://data.cma.cn/site/index.html). The multi-decadal convection-permitting WRF simulations were performed using the China's Tianhe-2 supercomputer at the National Supercomputer Center in Guangzhou.

References

Bao J, Feng J, Wang Y (2015) Dynamical downscaling simulation and future projection of precipitation over China. J Geophys Res Atmos 120:8227–8243. doi:10.1002/2015JD023275

Bennett JC, Wang QJ, Li M, Robertson DE, Schepen A (2016) Reliable long-range ensemble streamflow forecasts: Combining calibrated climate forecasts with a conceptual runoff model and a staged error model. Water Resour Res 52:8238–8259. doi:10.1002/2016WR019193

Brisson E, Van Weverberg K, Demuzere M, Devis A, Saeed S, Stengel M, van Lipzig NPM (2016) How well can a convection-permitting climate model reproduce decadal statistics of precipitation, temperature and cloud characteristics? Clim Dyn 47:3043–3061. doi:10.1007/s00382-016-3012-z

Caldwell P, Chin HS, Bader DC et al. (2009) Evaluation of a WRF dynamical downscaling simulation over California. Clim Change 95:499–521. doi:10.1007/s10584-009-9583-5

Centre for Research on the Epidemiology of Disasters (2005) Centre for Research on the Epidemiology of Disasters. Data From EM-DAT, The International Disaster Database, Universite Catholique de Louvain, Brussels, Belgium.

Chan SC, Kendon EJ, Roberts N, Blenkinsop S, Fowler HJ (2018) Large-scale predictors for extreme hourly precipitation events in convection-permitting climate simulations. J Clim 31:2115–2131. doi:10.1175/JCLI-D-17-0404.1

Chen H, Wang S, Wang Y (2020) Exploring abrupt alternations between wet and dry conditions on the basis of historical observations and convection-permitting climate model simulations. J Geophys Res 125, e2019JD031982. doi:10.1029/2019JD031982

Clark PA, Roberts N, Lean H, Ballard SP, Charlton-Perez C (2016) Convection-permitting models: A step-change in rainfall forecasting. Meteor Appl 23, 165–181. doi.org/10.1002/met.1538

Di Luca A, de Elía R, Laprise R (2013) Potential for small scale added value of RCM's downscaled climate change signal. Clim Dyn 40:601–618. doi: 10.1007/s00382-012-1415-z

Dudhia J (1989) Numerical study of convection observed during the Winter Monsoon Experiment using a mesoscale two-dimensional model. J Atmos Sci 46:3077–3107. doi:10.1175/1520-0469(1989)046<3077:NSOCOD>2.0.CO;2

Fischer EM, Knutti R (2015) Anthropogenic contribution to global occurrence of heavy-precipitation and high-temperature extremes. Nat Clim Change 5:560–564. doi:10.1038/nclimate2617

Frei C, Scho¨ll R, Fukutome S, Schmidli J, Vidale PL (2006) Future change of precipitation extremes in Europe: An intercomparison of scenarios from regional climate models. J Geophys Res 111, D06105. doi:10.1029/2005JD005965

Gao Z, Wan R, Ye Q, et al. (2020) Typhoon Disaster Risk Assessment Based on Emergy Theory: A Case Study of Zhuhai City, Guangdong Province, China. Sustainability 12 (10): 4212. doi.org/10.3390/su12104212

Hallegatte S, Green C, Nicholls RJ, Corfee-Morlot J (2013) Future flood losses in major coastal cities. Nat Clim Change 3 (9), pp. 802-806. doi.org/10.1038/NCLIMATE1979

Hagemann S, Chen C, Haerter JO, Heinke J, Gerten D, Piani C (2011) Impact of a statistical bias correction on the projected hydrological changes obtained from three GCMs and two hydrology models. J Hydrometeor 12:556–578.

doi:10.1175/2011JHM1336.1

Heikkilä U, Sandvik A, Sorteberg A (2011) Dynamical downscaling of ERA-40 in complex terrain using the WRF regional climate model. Clim Dyn 37:1551–1564. doi:10.1007/s00382-010-0928-6

Hong SY, Pan HL (1996) Nonlocal boundary layer vertical diffusion in a medium-range forecast model. Mon Wea Rev 124:2322–2339. doi:10.1175/15200493(1996)124<2322:NBLVDI>2.0.CO;2

Hong SY, Noh Y, Dudhia J (2006) A new vertical diffusion package with an explicit treatment of entrainment processes. Mon Wea Rev 134:2318–2341. doi:10.1175/MWR3199.1

Huppert HE, Sparks RSJ (2006) Extreme natural hazards: population growth, globalization and environmental change. Philos T Soc A: Math, Phys Eng Sci 364 (1845): 1875-1888. doi.org/10.1098/rsta.2006.1803

Iacono MJ, Delamere JS, Mlawer EJ, Shephard MW, Clough SA, Collins WD (2008) Radiative forcing by long-lived greenhouse gases: Calculations with the AER radiative transfer models. J Geophys Res 113, D13103. doi:10.1029/2008JD009944

IPCC (2013) Climate change 2013 of the physical science basis. Working group I, the fifth assessment report of intergovernmental panel for climate change, summary for policy makers. IPCC Switzerland.

Ishida K, Tanaka K, Hama T (2020) Sensitivity analysis of convective parameterizations of a regional climate model in higher-resolution domains for long-term precipitation reconstruction. J Water Clim Change 11 (4): 1467–1480. doi.org/10.2166/wcc.2019.069

Jimenez PA, Dudhia JJ, Gonzalez-Rouco F, Navarro J, Montavez JP, Garcia-

Bustamante E (2012) A revised scheme for the WRF surface layer formulation. Mon Wea Rev 140:898–918. doi:10.1175/MWR-D-11-00056.1

Kain JS, Fritsch JM (1992) The role of the convective “trigger function” in numerical forecasts of mesoscale convective systems. Meteorl Atmos Phys 49:93–106. doi:10.1007/BF01025402

Kain JS (2004) The Kain–Fritsch convective parameterization: An update. J Appl Meteor 43:170–181. doi.org/10.1175/1520-0450(2004)043<0170:TKCPAU>2.0.CO;2

Kanamitsu M, Kanamaru H (2007) Fifty-seven-year California reanalysis downscaling at 10 km (CaRD10) Part I. System detail and validation with observations. J Clim 20:5527–5552. doi.org/10.1175/2007JCLI1482.1

Kang HS, Hong SY (2008) Sensitivity of the simulated East Asian summer monsoon climatology to four convective parameterization schemes. J Geophys Res: Atmos 113(D15). doi.org/10.1029/2007JD009692

Kendon EJ et al (2017) Do convection-permitting regional climate models improve projections of future precipitation change? Bull Amer Meteor Soc 79–93. doi:10.1175/BAMS-D-15-0004.1

Kim G, Cha D, Park C et al (2020) Evaluation and Projection of Regional Climate over East Asia in CORDEX-East Asia Phase I Experiment. Asia-Pacific J Atmos Sci. doi:10.1007/s13143-020-00180-8

Kirchmeier-Young MC, Zhang X (2020) Human influence has intensified extreme precipitation in North America. PNAS 117:13308–13313. doi:10.1073/pnas.1921628117

Kouadio K, Bastin S, Konare A, Ajayi VO (2020) Does convection-permitting simulate better rainfall distribution and extreme over Guinean coast and surroundings?

Clim Dyn 55:153–174. doi:10.1007/s00382-018-4308-y

Lavender SL, Walsh KJE (2011) Dynamically downscaled simulations of Australian region tropical cyclones in current and future climates. Geophys Res Lett 38, L10705. doi:10.1029/2011GL047499

Leutwyler D, Lüthi D, Ban N, Fuhrer O, Schär C (2017) Evaluation of the convection-resolving climate modeling approach on continental scales. J Geophys Res Atmos 122:5237–5258. doi:10.1002/2016JD026013

Lin Y, Farley R, Orville H (1983) Bulk parameterization of the snow filed in a cloud model. J Climate Appl Meteor 22:1065–1092. doi:10.1175/1520-0450(1983)022<1065:BPOTSF>2.0.CO;2

Liu C et al (2017) Continental-scale convection-permitting modeling of the current and future climate of North America. Clim Dyn 49:71–95. doi:10.1007/s00382-016-3327-9

Liu C, Ikeda K, Thompson G, Rasmussen R, Dudhia J (2011) High-resolution simulations of wintertime precipitation in the Colorado headwaters region: Sensitivity to physics parameterizations. Mon Wear Rev 139:3533–3553. doi:10.1175/MWR-D-11-00009.1

Lohmann U, Roeckner E (1996) Design and performance of a new cloud microphysics scheme developed for the ECHAM general circulation model. Clim Dyn 12:557–572. doi:10.1007/BF00207939

Mayhorn CB, McLaughlin AC (2014) Warning the world of extreme events: A global perspective on risk communication for natural and technological disaster. Saf Sci 61: 43-50. doi.org/10.1016/j.ssci.2012.04.014

Mlawer EJ, Taubman SJ, Brown PD, Iacono MJ, Clough SA (1997) Radiative transfer for inhomogeneous atmospheres: RRTM, a validated correlated-k model for the longwave. J Geophys Res 102:16663–16682. doi:10.1029/97JD00237

Miao C, Sun Q, Duan Q, Wang Y (2016) Joint analysis of changes in temperature and precipitation on the Loess Plateau during the period 1961–2011. Clim Dyn 47:3221–3234. doi:10.1007/s00382-016-3022-x

Morrison H, Gettelman A (2008) A New Two-Moment Bulk Stratiform Cloud Microphysics Scheme in the Community Atmosphere Model, Version 3 (CAM3). Part I: Description and Numerical Tests. J Climate 21:3642–3659. doi:10.1175/2008JCLI2105.1

Pfahl S, O'Gorman P, Fischer E (2017) Understanding the regional pattern of projected future changes in extreme precipitation. Nat Clim Change 7:423–427. doi:10.1038/nclimate3287

Prein AF et al. (2015) A review on regional convection-permitting climate modeling: Demonstrations, prospects, and challenges, Rev Geophys 53:323–361. doi:10.1002/2014RG000475.

Prein AF, Gobiet A (2016) Impacts of uncertainties in European gridded precipitation observations on regional climate analysis. Int J Climatol 37:305–327. doi:10.1002/joc.4706. doi:10.1002/joc.4706

Prein AF, Rasmussen RM, Ikeda K, Liu C, Clark MP, Holland GJ (2017) The future intensification of hourly precipitation extremes. Nat Clim Change 7:48–52. doi:10.1038/nclimate3168

Qiu L, Im ES, Hur J, et al. (2020) Added value of very high resolution climate simulations over South Korea using WRF modeling system. Clim Dyn 54, 173–189. doi.org/10.1007/s00382-019-04992-x

Riahi K, Rao S, Krey V, et al. (2011) RCP 8.5−A scenario of comparatively high greenhouse gas emissions. Clim Change 109, 33. doi.org/10.1007/s10584-011-

0149-y

Rasmussen R, Ikeda K, Liu C, Gochis D, Clark M, Dai A, Zhang G (2014) Climate change impacts on the water balance of the Colorado headwaters: High-resolution regional climate model simulations. J Hydrometeor 15:1091–1116. doi:10.1175/JHM-D-13-0118.1

Salathe´ EP Jr, R Steed, CF Mass, PH Zahn (2008) A high-resolution climate model for the U.S. Pacific Northwest: Mesoscale feedbacks and local responses to climate change. J Climate 21:5708–5726. doi:10.1175/2008JCLI2090.1

Silverman NL, Maneta MP, Chen SH, Harper JT (2013) Dynamically downscaled winter precipitation over complex terrain of the central Rockies of western Montana, USA. Water Resour Res 49:458–470. doi:10.1029/2012WR012874

Skamarock WC, Klemp JB, Dudhia J, Gill DO, Barker DM, Wang W, Powers JG (2005) A description of the Advanced Research WRF version 2. NCAR Tech. Note NCAR/TN-468+STR, 88 pp. doi.org/10.5065/D6DZ069T

Soares PMM, Cardoso RM, Semedo Á, Chinita MJ, Ranjha R (2014) Climatology of the Iberia coastal low-level wind jet: weather research forecasting model high-resolution results, Tellus Series A. Dynamic Meteorology and Oceanography 66:22377–18. doi:10.3402/tellusa.v66.22377

Svensson C, Brookshaw A, Scaife AA, Bell VA, Mackay JD, Jackson CR, Hannaford J, Davies HN, Arribas A, Stanley S (2015) Long-range forecasts of UK winter hydrology. Environ Res Lett 10:064006. doi:10.1088/1748-9326/10/6/064006

Swiss Re, 2013. Mind the risk: a global ranking of cities under threat from natural disasters. Switzerland: Swiss Re.

Wang S, Wang Y (2019) Improving probabilistic hydroclimatic projections through high-resolution convection-permitting climate modeling and Markov chain

Monte Carlo simulations. Clim Dyn 53:1613–1636. doi:10.1007/s00382-019-04702-7

Wang S, Zhu J (2020) Amplified or exaggerated changes in perceived temperature extremes under global warming. Clim Dyn 54:117–127. doi:10.1007/s00382-019-04994-9

Wang Y, Geerts B, Liu C (2018) A 30-year convection-permitting regional climate simulation over the interior western United States. Part I: Validation. Int J Climatol 1–21. doi:10.1002/joc.5527

Wagner A, Heinzeller D, Wagner S, Rummler T, Kunstmann H (2018) Explicit convection and scale-aware cumulus parameterizations: High-resolution simulations over areas of different topography in Germany. Mon Wea Rev 146:1925–1944. doi:10.1175/MWR-D-17-0238.1

White CJ et al (2013) On regional dynamical downscaling for the assessment and projection of temperature and precipitation extremes across Tasmania, Australia. Clim Dyn 41:3145–3165. doi:10.1007/s00382-013-1718-8

Yatagai A, Kamiguchi K, Arakawa O, Hamada A, Yasutomi N, Kitoh A (2012) APHRODITE: Constructing a long-term daily gridded precipitation dataset for Asia based on a dense network of rain gauges. Bull Amer Meteorol Soc 93: 1401–1415. doi:10.1175/BAMS-D-11-00122.1

Yu E, Sun J, Chen H, Xiang W (2015) Evaluation of a high-resolution historical simulation over China: Climatology and extremes. Clim Dyn 45:2013–2031. doi:10.1007/s00382-014-2452-6

Zhang B, Wang S, Wang Y (2019) Copula-based convection-permitting projections of future changes in multivariate drought characteristics. J Geophys Res 124:7460–7483. doi:10.1029/2019JD030686

Zhu J, Wang S, Huang G (2019) Assessing climate change impacts on human-perceived temperature extremes and underlying uncertainties. J Geophys Res 124:3800–3821. doi:10.1029/2018JD029444

Zittis G, Bruggeman A, Camera C, et al (2017) The added value of convection permitting simulations of extreme precipitation events over the eastern Mediterranean. Atmos res 191: 20-33. doi.org/10.1016/j.atmosres.2017.03.002

List of Figure Captions

Figure 1. (a) The WRF model domain with three nested grids (D01, D02, and D03) and terrain heights (m). The horizontal grid spacings of three nested grids include 36 km (D01), 12 km (D02), and 4 km (D03), respectively. (b) The innermost domain D03 (GBA) with the 4-km resolution includes the Guangdong-Hong Kong-Macao Greater Bay Area (indicated in red line) and surroundings.

Figure 2. Temporal variations of daily temperature and precipitation simulated using different microphysics parameterizations for the summer season from June 1, 1981 to August 31, 1981.

Figure 3. The web layout of China's Greater Bay Area Climate Data Portal (GBAcdp).

Figure 4. Spatial distributions of (a, b, c) absolute and (d, e, f) relative model biases for average daily precipitation simulations with 36-, 12- and 4-km resolutions. Δ denotes the domain-averaged bias between simulations at different resolutions and observation during the period of 1980 − 2005.

Figure 5. (a) Absolute model biases of seasonal precipitation. (b) Boxplots of seasonal daily precipitation.

Figure 6. Comparison of seasonal precipitation simulations across different spatial resolutions during 1980–2005.

Figure 7. Comparison of simulated and observed average monthly and annual precipitation.

Figure 8. Spatial distributions of (a, b, c) absolute and (d, e, f) relative model biases for daily mean temperature simulations with 36-, 12- and 4-km resolutions. Δ denotes the domain-averaged bias.

Figure 9. (a) Absolute model biases of seasonal mean temperature. (b) Boxplots of seasonal mean temperature.

Figure 10. Comparison of simulated and observed monthly and annual mean temperatures.

Figure 11. The added values (AVs) of the WRF-4km simulations of annual and summer precipitation (a, b, c, d) and temperature (e, f, g, h) relative to the WRF-12km and WRF-36km simulations. The weather station data is used as a reference dataset.

Figure 12. Average values of precipitation indices (a, b, c, d) SDII and (e, f, g, h) CWD derived from the WRF-36km, WRF-12km and WRF-4km simulations, as well as the observation.

Figure 13. Frequencies of simulated and observed daily precipitation with different intensities (unit of axis x: mm/day).

Figure 14. Average values of temperature indices (a, b, c, d) SU and (e, f, g, h) CSU derived from the WRF-36km, WRF-12km and WRF-4km simulations, as well as the observation.

Figure 15. Frequencies of simulated and observed daily mean temperatures (unit of axis x: °C).

Figure 16. Spatial distributions of the percentage changes in the annual and seasonal precipitation during the future period of 2074−2099 relative to the period of 1980–2005.

Figure 17. Spatial distributions of the changes in the annual and seasonal temperature by the end of the 21st century relative to the period of 1980–2005.

Figure 18. Spatial distributions of the changes in the precipitation and temperature indices by the end of the 21st century relative to the period of 1980–2005.

List of Table Captions

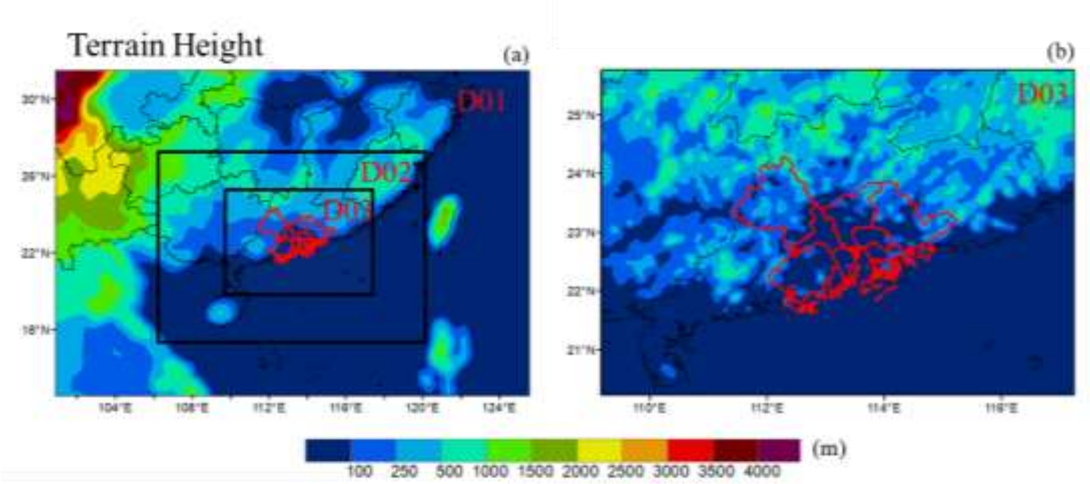

Figure 1. (a) The WRF model domain with three nested grids (D01, D02, and D03) and terrain heights (m). The horizontal grid spacings of three nested grids include 36 km (D01), 12 km (D02), and 4 km (D03), respectively. (b) The innermost domain D03 (GBA) with the 4-km resolution includes the Guangdong-Hong Kong-Macao Greater Bay Area (indicated in red line) and surroundings.

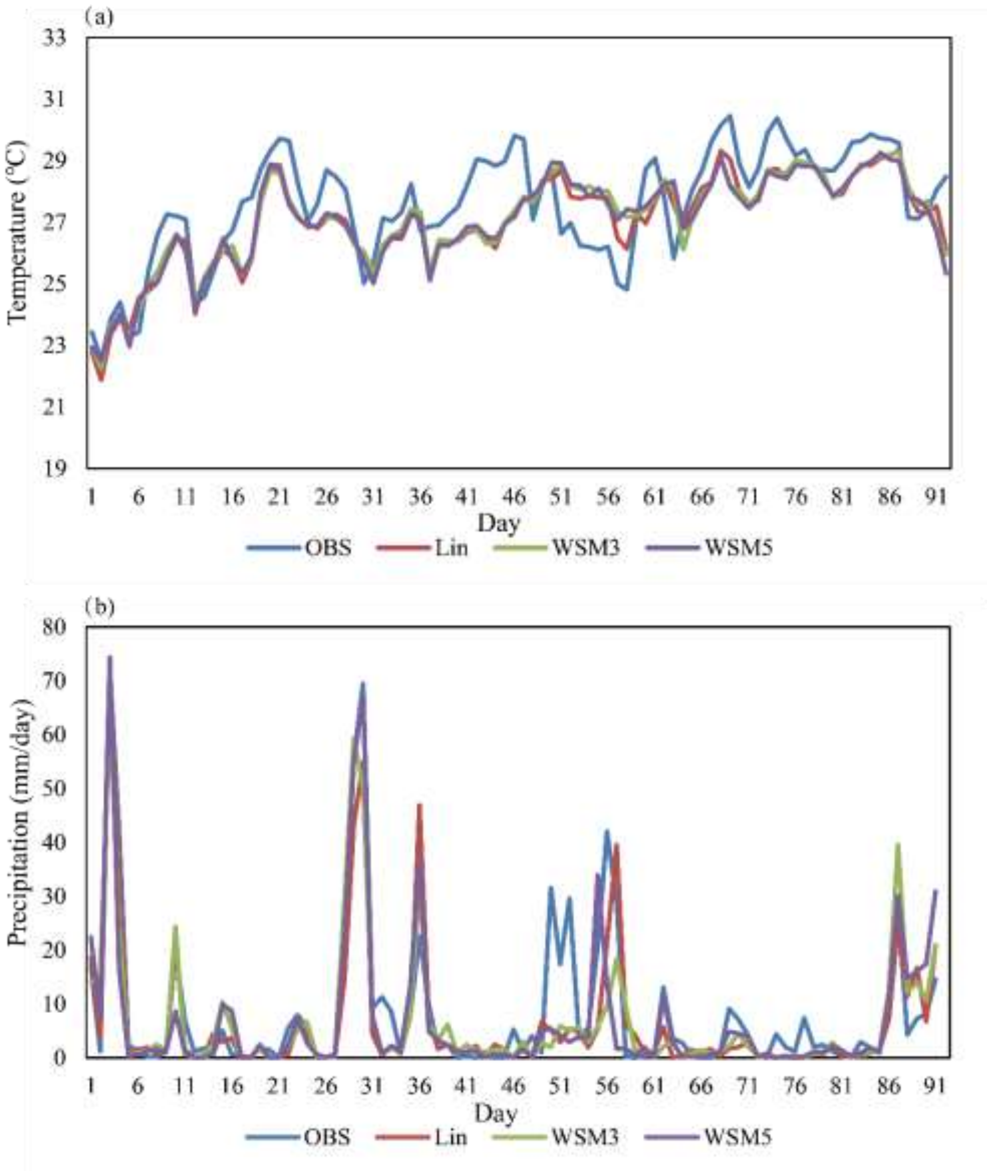

Figure 2. Temporal variations of daily temperature and precipitation simulated using different microphysics parameterizations for the summer season from June 1, 1981 to August 31, 1981.

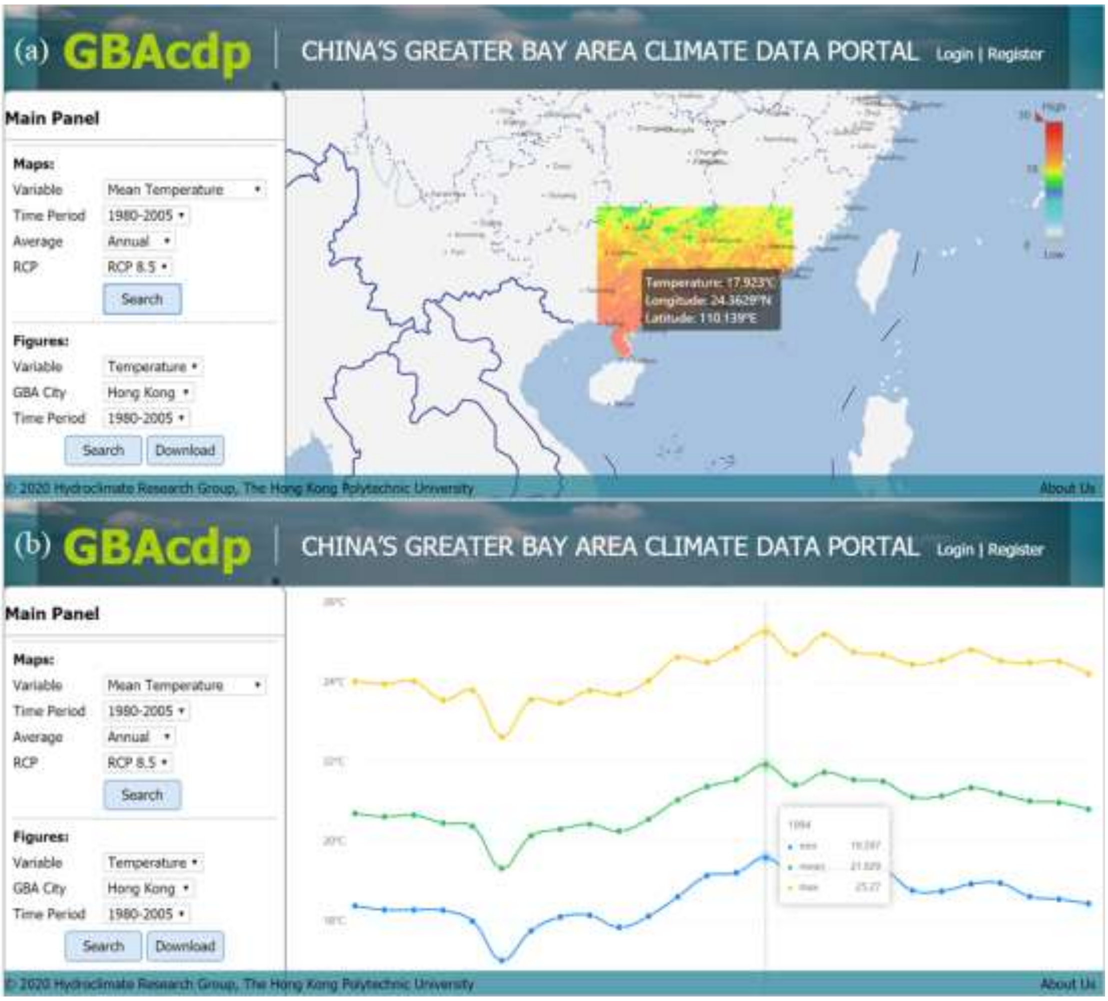

Figure 3. The web layout of China's Greater Bay Area Climate Data Portal (GBAcdp).

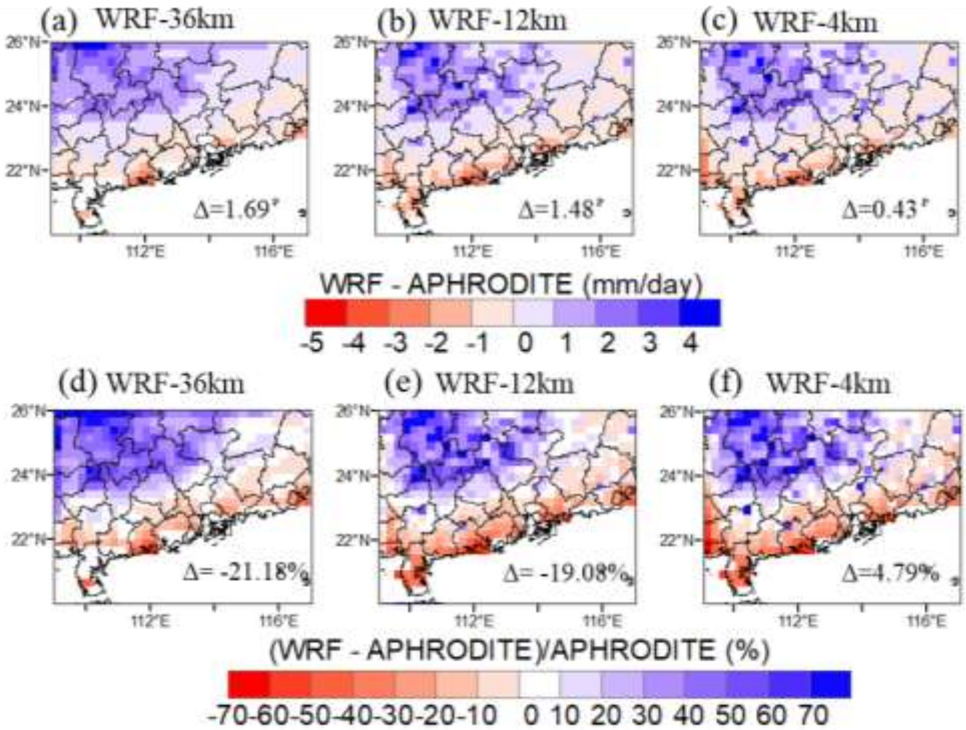

Figure 4. Spatial distributions of (a, b, c) absolute and (d, e, f) relative model biases for average daily precipitation simulations with 36-, 12- and 4-km resolutions. Δ denotes the domain-averaged bias between simulations at different resolutions and observation during the period of 1980 − 2005.

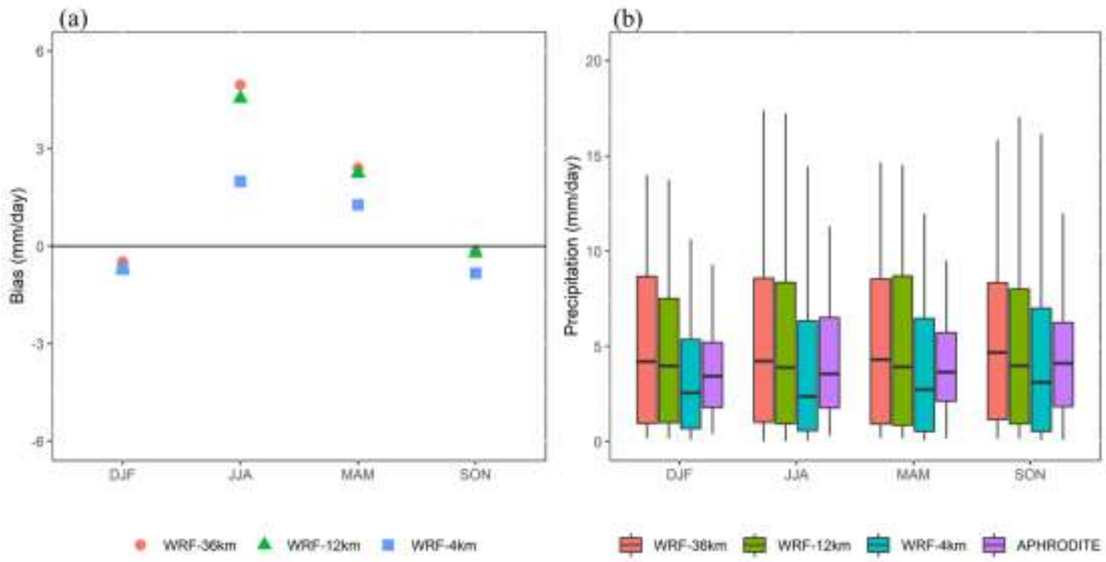

Figure 5. (a) Absolute model biases of seasonal precipitation. (b) Boxplots of seasonal daily precipitation.

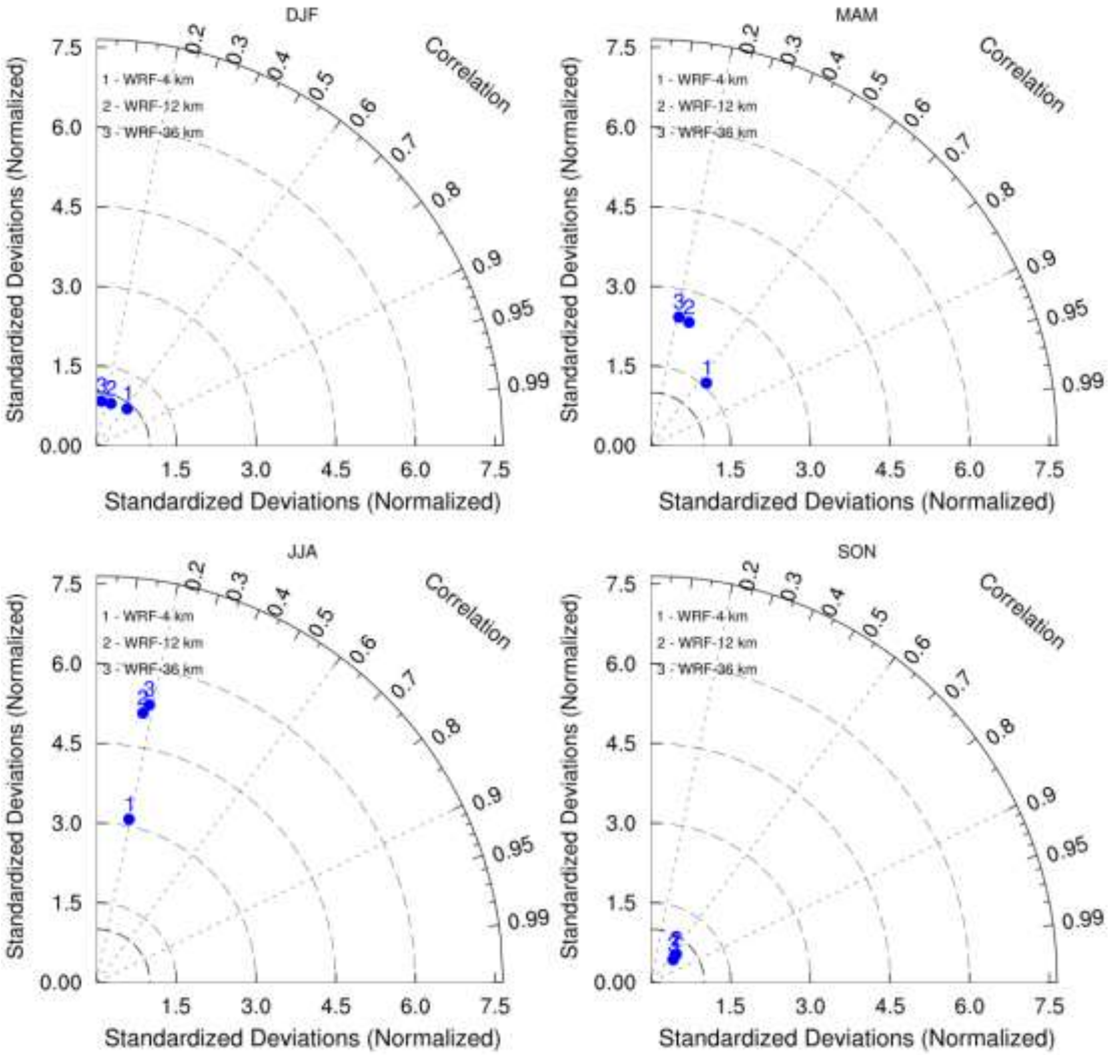

Figure 6. Comparison of seasonal precipitation simulations across different spatial resolutions during 1980–2005.

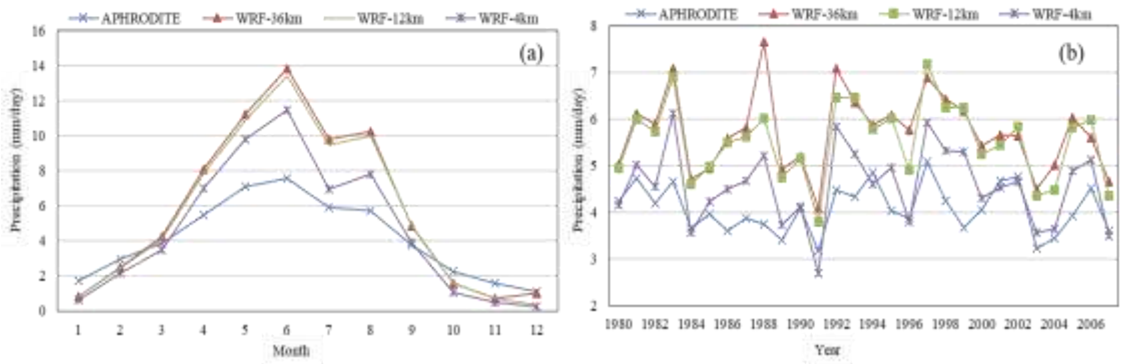

Figure 7. Comparison of simulated and observed average monthly and annual precipitation.

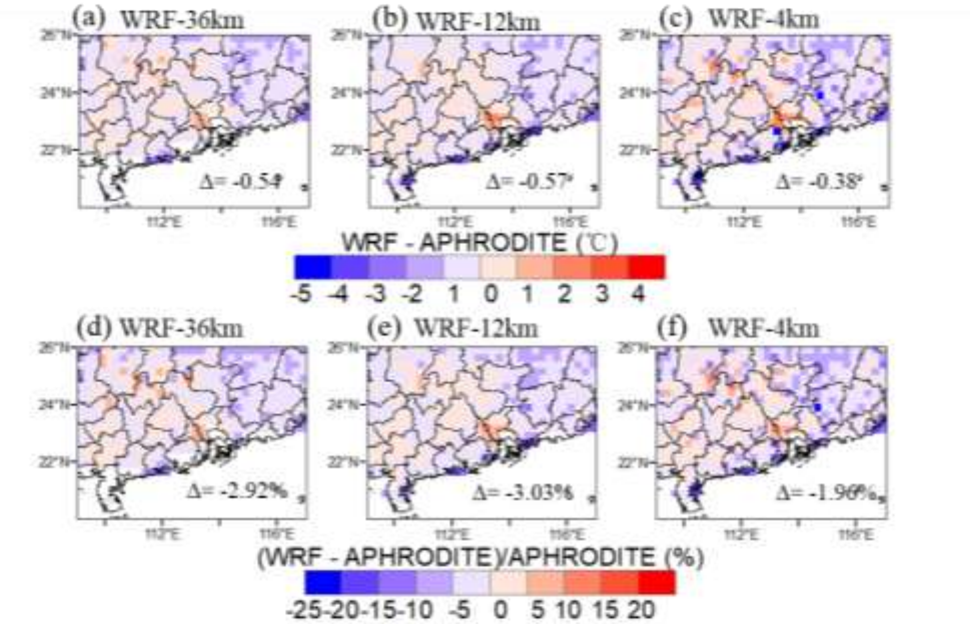

Figure 8. Spatial distributions of (a, b, c) absolute and (d, e, f) relative model biases for daily mean temperature simulations with 36-, 12- and 4-km resolutions. Δ denotes the domain-averaged bias.

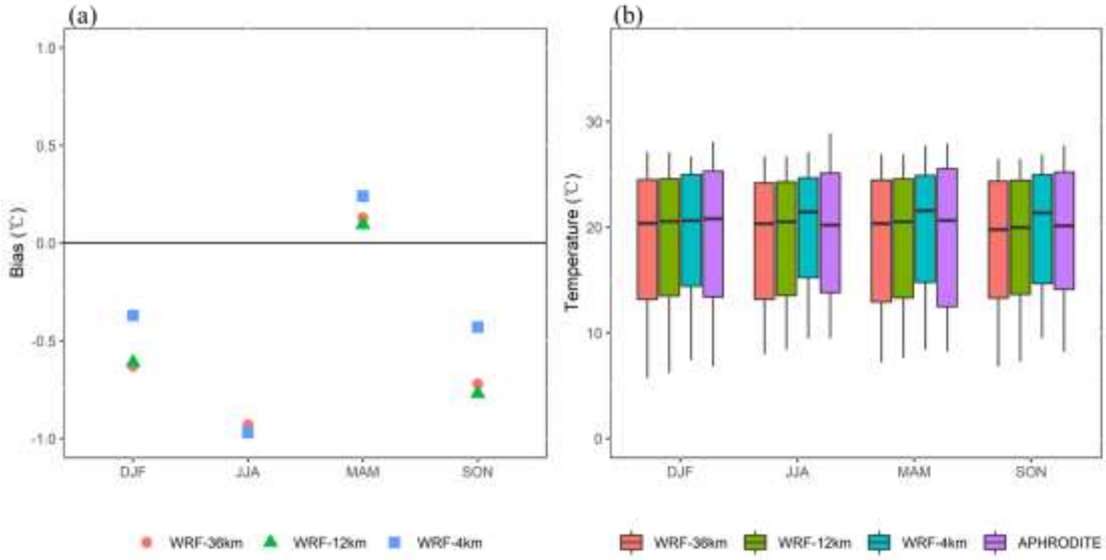

Figure 9. (a) Absolute model biases of seasonal mean temperature. (b) Boxplots of seasonal mean temperature.

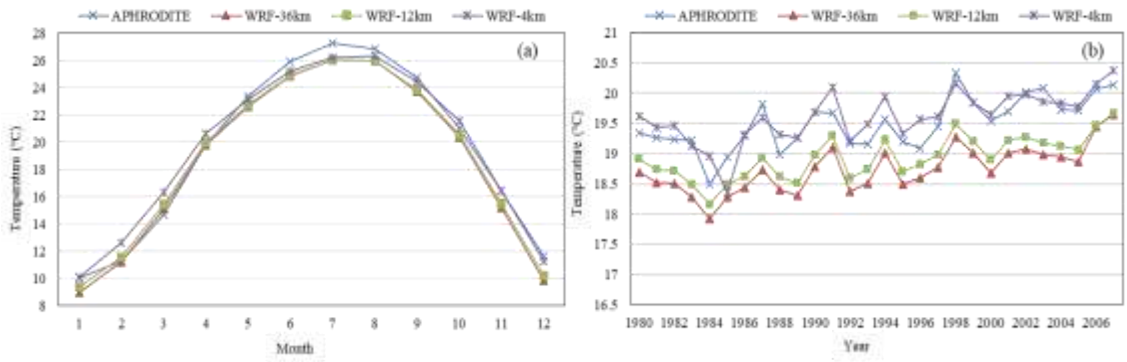

Figure 10. Comparison of simulated and observed monthly and annual mean temperatures.

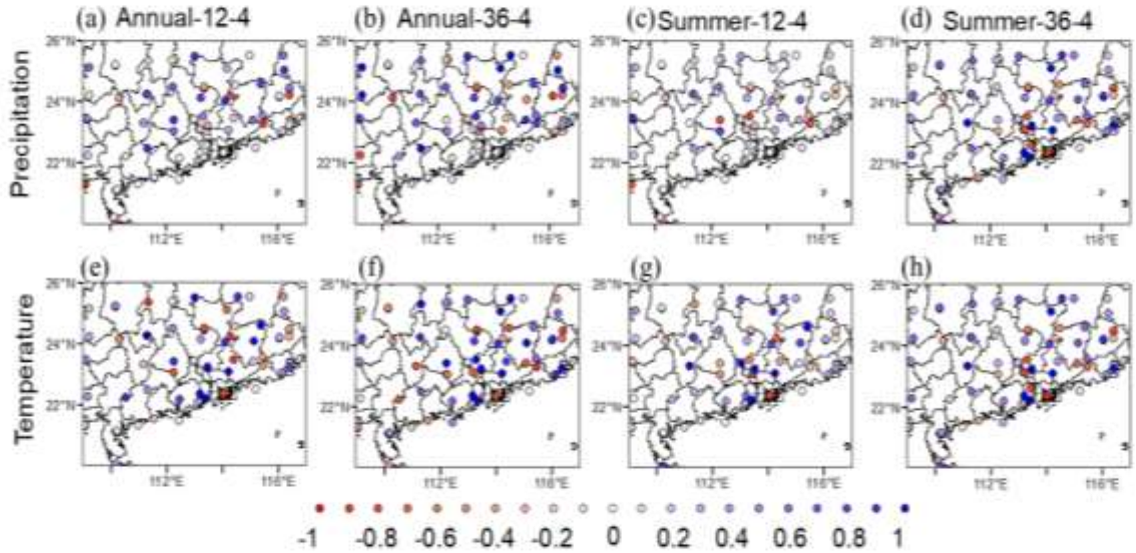

Figure 11. The added values (AVs) of the WRF-4km simulations of annual and summer precipitation (a, b, c, d) and temperature (e, f, g, h) relative to the WRF-12km and WRF-36km simulations. The weather station data is used as a reference dataset.

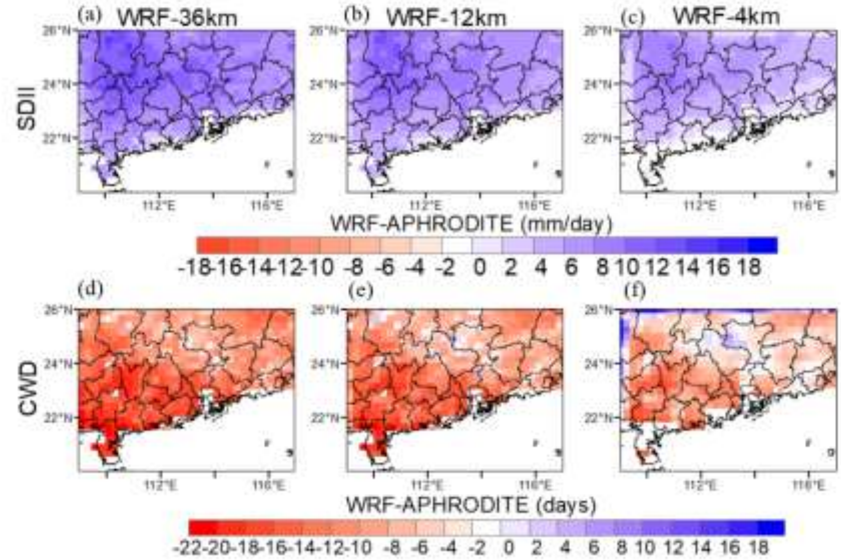

Figure 12. Spatial distributions of absolute model biases for average values of precipitation indices (a, b, c) SDII and (d, e, f) CWD for WRF-36km, WRF-12km and WRF-4km, as well as the observation.

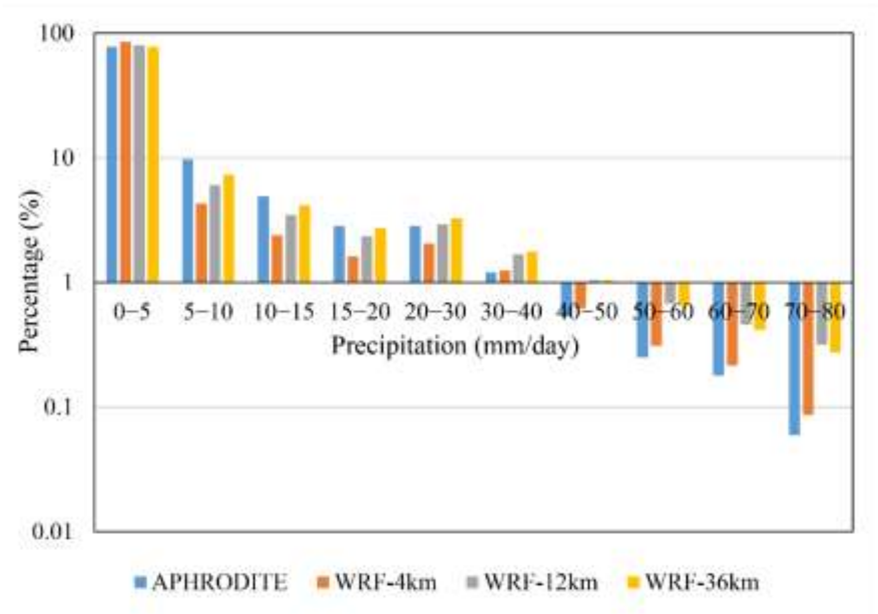

Figure 13. Frequencies of simulated and observed daily precipitation with different intensities (unit of axis x: mm/day).

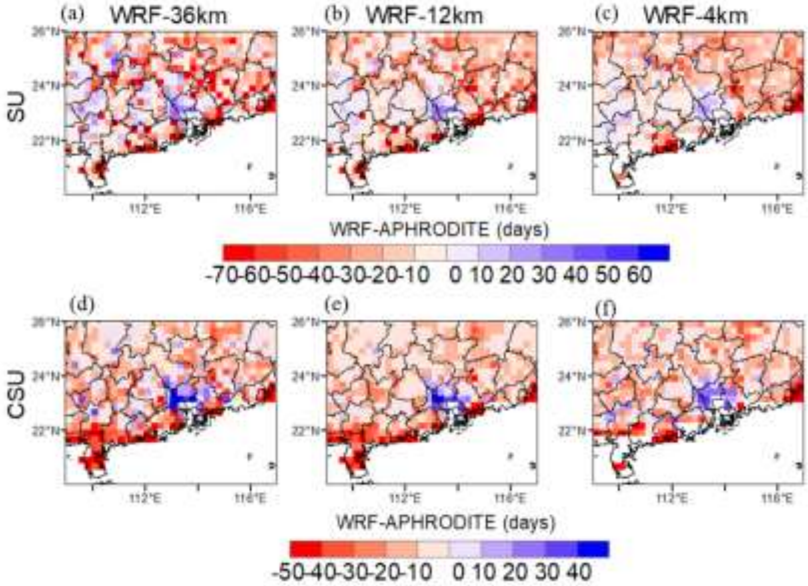

Figure 14. Spatial distributions of absolute model biases for average values of temperature indices (a, b, c) SU and (d, e, f) CSU derived from the WRF-36km, WRF-12km and WRF-4km simulations, as well as the observation.

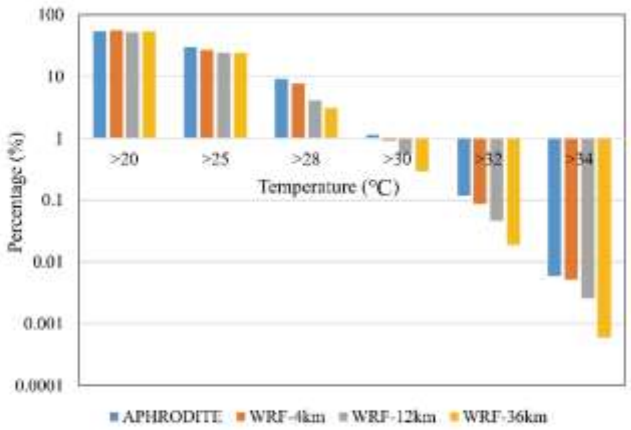

Figure 15. Frequencies of simulated and observed daily mean temperatures (unit of axis x: ℃).

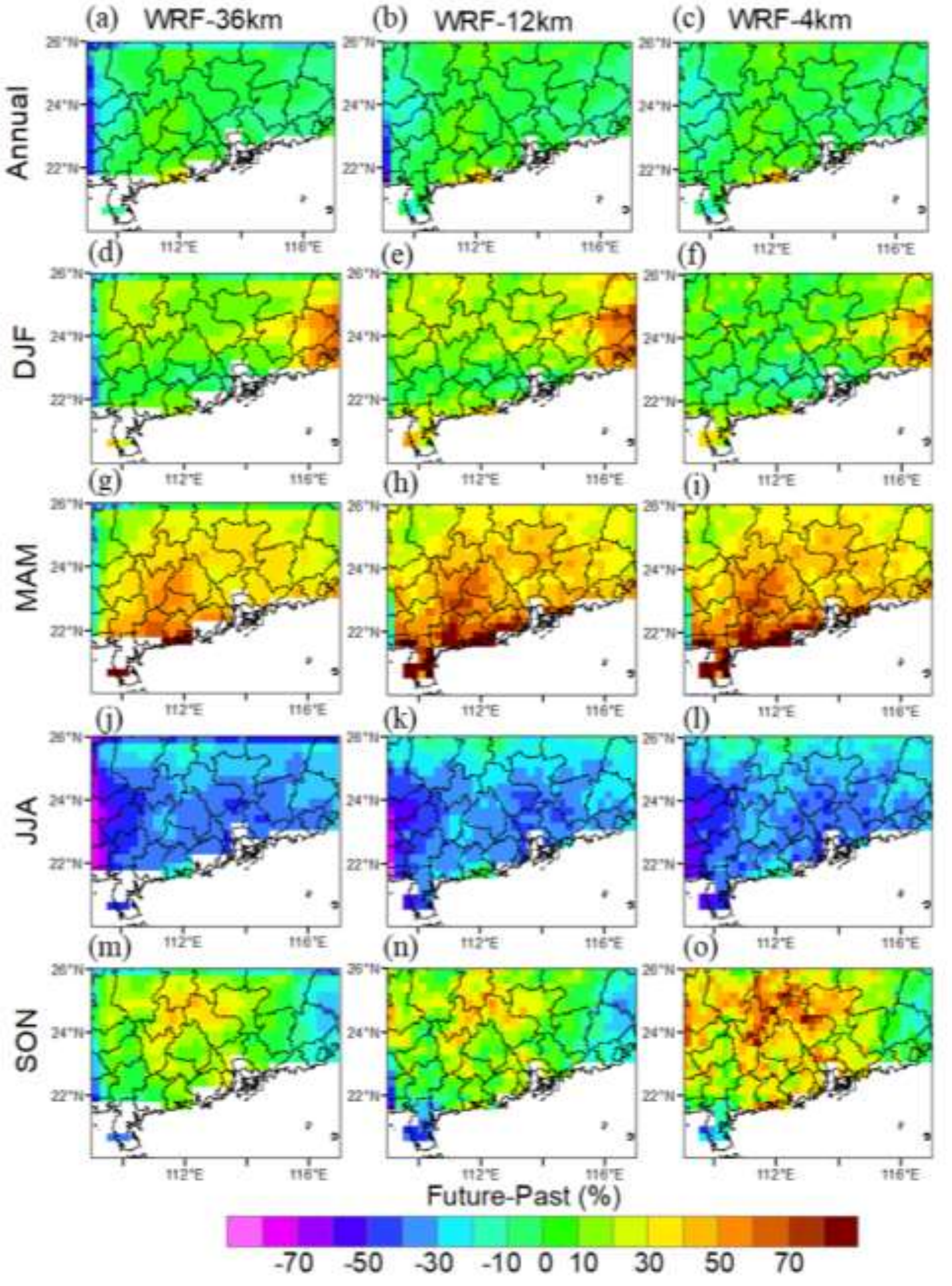

Figure 16. Spatial distributions of the percentage changes in the annual and seasonal precipitation during the future period of 2074−2099 relative to the period of 1980–2005.

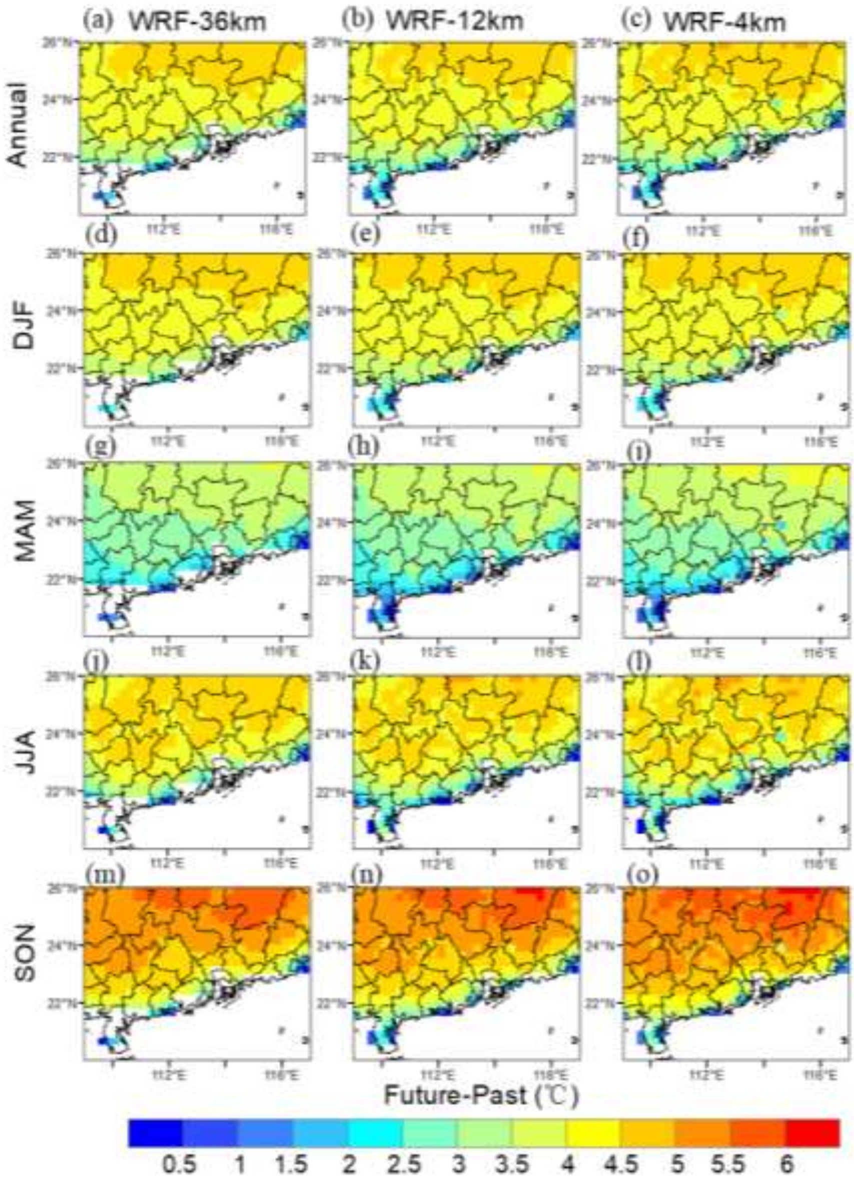

Figure 17. Spatial distributions of the changes in the annual and seasonal temperature by the end of the 21st century relative to the period of 1980–2005.

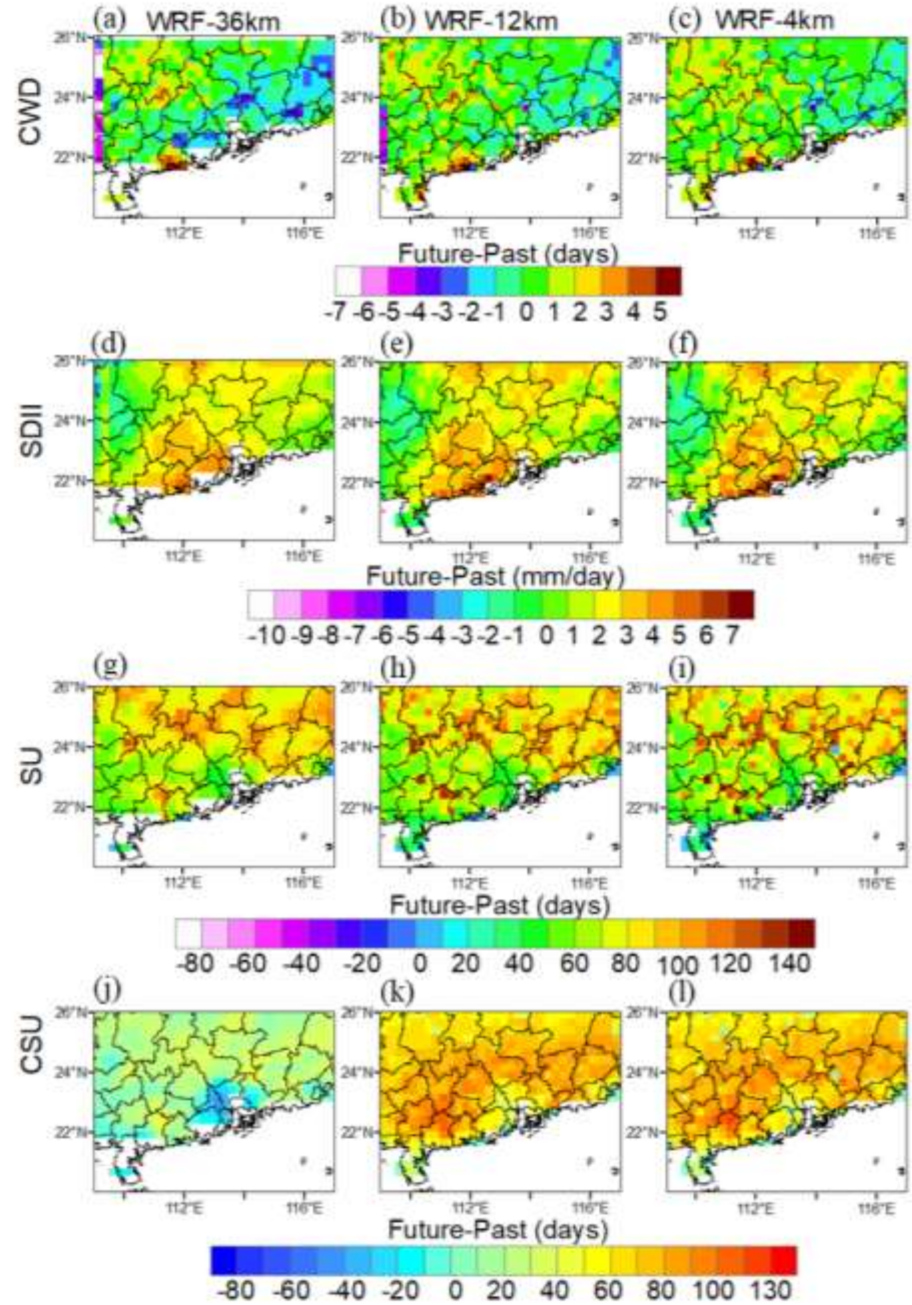

Figure 18. Spatial distributions of the changes in the precipitation and temperature indices by the end of the 21st century relative to the period of 1980–2005.

Table 1 Extreme precipitation and temperature indices

Category	Index	Descriptive name	Definitions	Units
Precipitation	SDII	Simple daily intensity index	The daily mean intensity of a time series of daily precipitation amounts at wet days	mm/day
	CWD	Consecutive wet days	The largest number of consecutive wet days of a time series of daily precipitation	days
Temperature	SU	Summer days	The number of days where TX > 25 ℃	days
	CSU	Consecutive summer days	The largest number of consecutive summer days of a time series of daily temperature	days

Table 2 Number of days for various categories of precipitation with different intensities

Time	Resolution	Wet days (above 1 mm/day)	Light rain (1-10 mm/day)	Medium rain (10-25 mm/day)	Large rain (25-50 mm/day)	Heavy rain (50-80 mm/day)	Extreme heavy rain (above 80 mm/day)
1980-2005	WRF-4km	92.1	54.0	19.1	10.9	4.6	3.6
	WRF-12km	121.3	70.2	27.6	14.6	4.3	3.5
	WRF-36km	142.0	73.1	32.8	15.9	4.1	2.7
2074-2099	WRF-4km	87.7	50.7	17.4	10.3	4.8	4.4
	WRF-12km	90.8	57.6	16.9	9.3	4.5	3.2
	WRF-36km	101.5	65.7	19.0	10.0	4.1	2.8